AGN feedback through multiple jet cycles in the Seyfert galaxy NGC 2639

Vaishnav V. Rao [1]★ P. Kharb,[2] Rubinur K.,[3] Silpa S.,[2] N. Roy,[4] B. Sebastian,[5] V. Singh,[6] J. Baghel,[2] S. Manna[2] and C. H. Ishwara-Chandra[2]

[1]*Indian Institute of Technology Bombay, Powai, Mumbai 400076, India*
[2]*National Centre for Radio Astrophysics (NCRA) – Tata Institute of Fundamental Research (TIFR), S. P. Pune University Campus, Ganeshkhind, Pune 411007, India*
[3]*Institute of Theoretical Astrophysics, University of Oslo, P.O. box 1029 Blindern, 0315 OSLO, Norway*
[4]*Johns Hopkins University, Department of Physics & Astronomy, 3400 N. Charles Street, Baltimore, MD 21218, USA*
[5]*Department of Physics and Astronomy, University of Manitoba, Winnipeg, MB R3T 2N2, Canada*
[6]*Astronomy and Astrophysics Division, Physical Research Laboratory, Ahmedabad 380009, India*

ABSTRACT

The Seyfert galaxy NGC 2639 was known to exhibit three episodes of active galactic nuclei (AGN) jet/lobe activity. We present here the upgraded *Giant Metrewave Radio Telescope* (uGMRT) 735 MHz image of NGC 2639 showing a fourth episode as witnessed by the discovery of $\sim$9 kpc radio lobes misaligned with the previously known $\sim$1.5 kpc, $\sim$360 pc, and $\sim$3 pc jet features detected through the Karl G. Jansky Very Large Array (VLA) and the Very Long Baseline Array (VLBA), respectively. Using the spectral ageing software BRATS, we derive the ages of the $\sim$9 kpc, $\sim$1.5 kpc, and $\sim$360 pc episodes to be, respectively, 34^{+4}_{-6}, $11.8^{+1.7}_{-1.4}$, and $2.8^{+0.7}_{-0.5}$ Myr, and conclude that minor mergers occurred $9-22$ Myr apart. NGC 2639 shows a deficit of molecular gas in its central $\sim$6 kpc region. The *GALEX NUV* image also shows a deficiency of recent star formation in the same region, while the star formation rate surface density in NGC 2639 is lower by a factor of $5-18$ compared to the global Schmidt law of star-forming galaxies. This makes NGC 2639 a rare case of a Seyfert galaxy showing episodic jet activity and possible signatures of jet-driven AGN feedback.

Key words: techniques: interferometric – galaxies: jets – galaxies: Seyfert – radio continuum: galaxies – galaxies: star formation – galaxies: active.

1 INTRODUCTION

Active galactic nuclei (AGNs) are the high-luminosity, energetic centres of galaxies that are dominated by light emitted from matter accreting on to a supermassive black hole (SMBH, $M_{BH} \sim 10^6 - 10^9$ M$_\odot$; Rees 1984; Padovani et al. 2017). In a small fraction of AGN (~ 10 per cent), relativistic jets are launched from the SMBH up to hundreds of kpc to even Mpc scales (Readhead, Cohen & Blandford 1978; Orr & Browne 1982; Heckman & Best 2014). AGNs have been historically broadly classified into Seyfert galaxies and quasars, with the fundamental difference lying in their bolometric luminosity (L_{bol}) with $L_{bol} \leq 10^{12}$ L$_\odot$ for Seyfert galaxies and higher for quasars (Schmidt & Green 1983; Soifer et al. 1987). Based on the presence or absence of broad bases to permitted emission lines in the optical spectra, Seyfert galaxies are further classified into types 1 and 2 (Khachikian & Weedman 1974; Hickox & Alexander 2018). It is widely believed that different viewing angles of the central engine surrounded by an obscuring torus explain the two Seyfert classes, with type 1s being viewed nearly face on, although there are several exceptions (Antonucci 1993; Ho 2008; Netzer 2015). Seyfert galaxies are primarily classified as 'radio-quiet' (RQ) AGN. Based on 6 GHz Karl G. Jansky Very Large Array *(VLA)* observations of Sloan Digital Sky Survey (SDSS) quasi-stellar objects, Kellermann

et al. (2016) have suggested RQAGN to be those having $21 \leq \log[L_6(\mathrm{W\ Hz^{-1}})] \leq 23$.

Outflows in Seyfert galaxies are not a well-understood phenomenon (Panessa et al. 2019). Only sensitive radio observations reveal the presence of radio structures with typical extents $\sim$10 kpc in Seyfert galaxies. Gallimore et al. (2006); Singh et al. (2015) found that $\gtrsim 40$ per cent of Seyfert galaxies in statistically large samples exhibit kiloparsec-scale radio structures (KSRs). It is unclear how these radio outflows are generated. The contribution of the AGN versus star formation to the radio emission is being debated (e.g. Baum et al. 1993; Hota & Saikia 2006; Sebastian et al. 2020). Several authors (Malzac, Beloborodov & Poutanen 2001; Markoff, Nowak & Wilms 2005; Behar et al. 2015; Kharb et al. 2015; Wong et al. 2016) have argued the case for Seyfert outflows being outflowing accretion disc coronae. High-resolution Very Long Baseline Array (VLBA) observations, on the other hand, have detected the presence of parsec-scale jets in a majority of radio-bright Seyfert galaxies (e.g. Thean et al. 2001; Nagar, Falcke & Wilson 2005; Kharb et al. 2010, 2021; Mezcua & Prieto 2014; Baldi et al. 2018), making a strong case for Seyfert galaxies being jetted AGN. Ho (2008) have argued that small collimated outflows in low-luminosity AGN like Seyferts can be agents of radiative or mechanical AGN feedback and this energy injection can lead to unsteady, intermittent accretion with a short duty cycle.

★ E-mail: vvrao@umich.edu

AGNs are believed to regulate galaxy growth by injecting energy into the surrounding gas which has the effect of either heating and/or expelling star-forming material ('negative feedback') or facilitating localized star formation ('positive feedback') (Alexander & Hickox 2012; Fabian 2012; Harrison 2017; Morganti 2017). While AGN 'feedback' is believed to be a fundamental process of galaxy formation, there are many outstanding questions from an observational point of view. AGN feedback has been suggested to come in the 'quasar mode' or the 'maintenance/jet mode' (e.g. Croton 2009; Bower, Benson & Crain 2012). The former is associated with radiatively driven AGN, where the energetic photons coupled with the surrounding gas drive high-velocity winds through the host galaxy and result in the removal of the star-forming material (e.g. Faucher-Giguère & Quataert 2012; Costa et al. 2018), while the latter is associated with AGN hosting radio jets that can transfer mechanical power (jets could heat, shock or entrain gas) and regulate star formation (e.g. McNamara & Nulsen 2012; Mahony et al. 2013; Morganti 2017; Hardcastle & Croston 2020). While highly collimated jets might not be efficient agents of AGN 'feedback', presumably due to the smaller working surfaces at their advancing ends, relatively isotropic impacts via changes in jet direction can be highly effective (King & Pounds 2015). Moreover, the contribution of jets towards the total AGN energy budget has been suggested to be ≲20 per cent (Merloni & Heinz 2008; Shankar et al. 2008; Cattaneo & Best 2009).

Sanders (1984) has argued that individual Seyfert activity episodes typically have a shorter duration than the minimum statistical lifetime of Seyfert activity in a particular galaxy ($3-7 \times 10^8$ yr), which would imply that the nuclei evolve through at least a 100 recurring Seyfert episodes. If it is assumed that Seyfert episodes in a particular galaxy are due to accretion on to the central black hole (BH), the short lifetime of Seyfert events would require separate episodes to be caused by distinct accretion events. Recent studies from the SDSS, though, have suggested that accretion rate changes are common within a given Seyfert duty cycle, producing a much more complex picture of accretion in Seyfert galaxies (Elitzur, Ho & Trump 2014; Koulouridis 2014; Koulouridis et al. 2016). So far, only a handful of Seyfert galaxies such as Mrk 6 (Kharb et al. 2006) and NGC 2992 (Irwin et al. 2016) have been known to exhibit multiple kpc-scale radio lobes, with Mrk 6 showing three jet episodes. Here and in other cases discussed in this paper, different jet 'episodes' are defined by surface brightness discontinuities, with each jet episode being delineated by the presence of either terminal hotspot-like features or lobes with well-defined edges, i.e. surface brightness discontinuity of the edges is at least three times the rms noise. Saikia (2022) has pointed out that different jets are also characterized by significant differences in position angle (PA; measured here from north through east with north being at $0°$) and differences in the steepness of the spectral index.

Interestingly, Sebastian et al. (2020) found tentative evidence for multiple episodes in a majority (5/9) of their Seyfert galaxy sample. This fraction was higher than that observed in radio galaxies ($\sim 10 - 15$ per cent; Jurlin et al. 2020) and was consistent with the theoretical expectation of Sanders (1984). Therefore, the rarity of known Seyfert galaxies with episodic activity may not be due to a true absence but rather due to the difficulty in their identification due to the low surface brightness of their lobes, small spatial extents, lack of collimation, and confusion with the radio emission from star formation. Hence, it is essential to design methods to identify various episodes of jetted emission in Seyfert galaxies to truly understand the life cycle of jets in these systems and their impact on the environment. Multifrequency, multiscale/resolution observations are one such method. Although

several AGNs, including radio galaxies and Seyfert galaxies, have been shown to exhibit two episodes of jet activity (see Saikia & Jamrozy 2009; Shabala et al. 2020; Saikia 2022, and references therein), it is scarce to find sources with three or more episodes (although see the simulations of Lalakos et al. 2022). Here, we report the discovery of a Seyfert galaxy NGC 2639, which shows four AGN jet activity episodes.

NGC 2639 (a.k.a UGC 4544) is a Seyfert 2 galaxy (Lacerda et al. 2020, see Fig. 1). At its redshift of 0.01113 (luminosity distance 48.2 Mpc), 1 arcsec corresponds to 0.229 kpc. NGC 2639 hosts water vapour megamasers most likely in a cool dense nuclear disc (Wilson, Braatz & Henkel 1995). The maser in this galaxy has a luminosity of 71 $L_\odot$ and has a prominent emission component of 3300 km s^{-1} (width 5.4 km s^{-1}) surrounded by some weaker emission components (Braatz, Wilson & Henkel 1994). Berrier et al. (2013) have estimated the mass of the BH in NGC 2639 using the $M_{BH} - \sigma$ relation (Ferrarese & Merritt 2000), which turns out to be $M_{BH} = (1.48 \pm 0.43) \times 10^8$ M$_\odot$. A more accurate BH mass is not yet available from the water vapour megamaser data due to the non-detection of 'satellite' lines, as described by Wilson et al. (1995). The stellar mass of the host galaxy has been estimated to be 1.48×10^{11} M$_\odot$ by Sweet et al. (2018). The Eddington ratio for the BH in NGC 2639 is obtained to be $\frac{L_{bol}}{L_{Edd}} = 4 \times 10^{-4}$, where L_{bol} is the bolometric luminosity and L_{Edd} is the Eddington luminosity. L_{bol} was obtained using the $2-10$ keV absorption-corrected X-ray luminosity $L_X = 46.6 \times 10^{40}$ erg s^{-1} for NGC 2639 (Terashima et al. 2002), and was estimated via the relation $L_{bol} = 15.8 L_X$ (see Ho 2009). The Eddington luminosity was obtained through $L_{Edd} = 1.26 \times 10^{38} \left(\frac{M_{BH}}{M_\odot} \right) = 1.86 \times 10^{46}$ erg s^{-1}. The extreme dimness of the nucleus, radiating well below the Eddington limit strongly suggests that the AGN accretion flow is radiatively inefficient in NGC 2639 (Heckman & Best 2014).

Using multiresolution radio observations with the VLA and the VLBA, Sebastian et al. (2019) reported three pairs of radio jets/lobes in NGC 2639. The three lobes are misaligned with each other without any apparent signatures of continuity. Sebastian et al. (2019) concluded that these three lobes were representative of three distinct episodes of AGN jet activity and ruled out other scenarios, including multiple jets from independent AGNs, slow jet precession, and jet bending due to pressure gradients within the galaxy. The presence of a jet precession was discounted based on the lack of supporting evidence for the continuity in flux densities or trajectories across the three distinct lobe pairs. Similarly, the likelihood of multiple independent jets originating from different AGNs was deemed implausible due to their extremely low probabilities. Lastly, pressure gradients were eliminated as a possibility due to the observed misalignment of the three lobes from the minor axis, which is incompatible with this hypothesis. However, it is worth noting that Xanthopoulos et al. (2010) have favoured jet-medium interaction rather than jet precession to explain the S-shaped, east-west MERLIN jet in NGC 2639 (corresponding to the 360 pc VLA jet; see ahead).

The jet extents of the three episodes were 1.5 kpc, 360 pc, and 3 pc as revealed by the VLA image at 5.5 GHz, historical VLA image at 5 GHz, and VLBA image at 8.3 GHz, respectively (see Fig. 2 and Table 1). Following the criterion of Kellermann et al. (2016), NGC 2639 is a RQAGN having log[L_6(W Hz^{-1})] = 22.15, obtained from its 5.5 GHz VLA lobes using a spectral index of -0.6. In this paper, we present new upgraded *Giant Metrewave Radio Telescope* (uGMRT; hereafter GMRT) images of NGC 2639 which reveal an additional set of radio lobes, not previously detected at GHz frequencies (see Fig. 1). This paper is divided as follows. In Section 2, we present the radio data analysis, followed by the spectral ageing
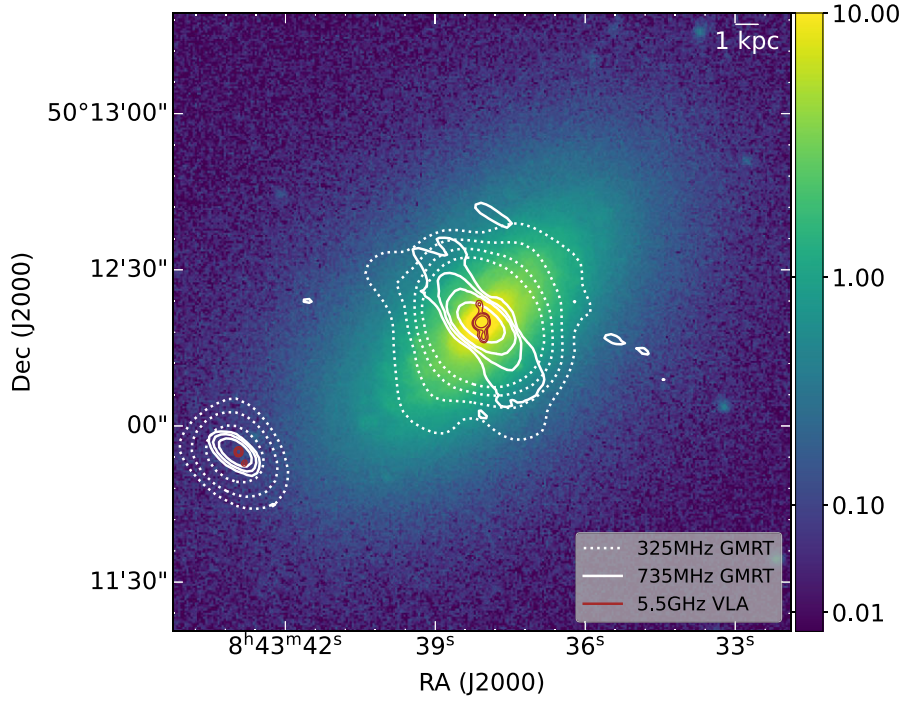
Figure 1. A radio-optical overlay of NGC 2639. The optical image comes from SDSS r band. The dotted, white contours represent the 325 MHz *Giant Metrewave Radio Telescope (*GMRT*)* data with contour levels (1, 2, 4, 8) × 1.6 mJy beam^{-1}. The solid white contours represent the 735 MHz GMRT data with contour levels (1, 2, 4, 32) × 0.6 mJy beam^{-1}. The solid brown contours come from the VLA 5.5 GHz image with contour levels (2, 4, 8, 64) × 0.03 mJy beam^{-1}.
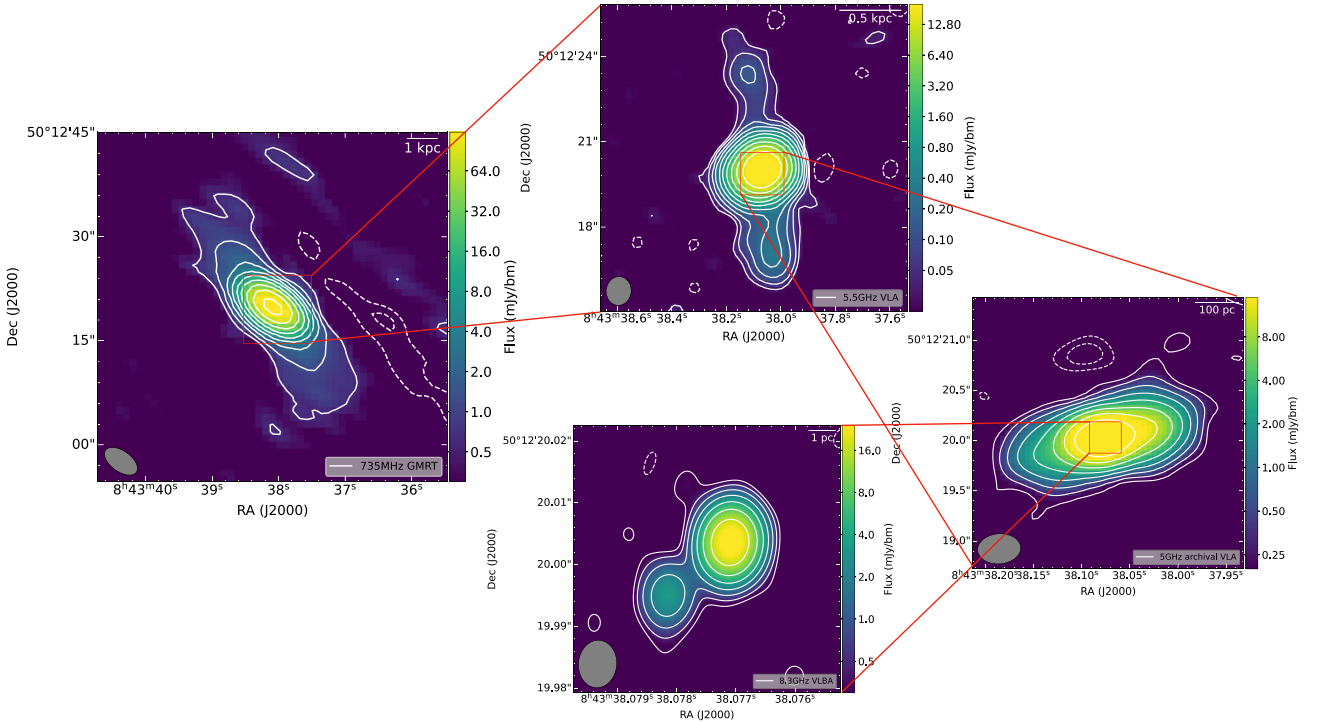

Figure 2. The four AGN jet episodes of NGC 2639. (*Left*) 735 MHz GMRT total intensity image. The ∼9 kpc north-east–south-west radio lobes at PA = 34° are seen in this image. Contour levels: (− 2, −1, 1, 2, 4, 8, 16, 32, 64, 128, 256) × 0.6 mJy beam^{-1}. Beam at the bottom left corner is of size: 5.48 arcsec × 3.0 arcsec at PA = 54.6°. (*Top*) 5.5 GHz *VLA* total intensity image. Contour levels: (− 2, −1, 1, 2, 4, 8, 16, 32, 64, 128, 256, 512) × 0.03 mJy beam^{-1}. The ∼1.5 kpc north–south radio jets at PA = 6° are seen here. Beam size: 1.02 arcsec × 0.89 arcsec at PA = −5.8°. (*Right*) 5 GHz *VLA* radio image. Contour levels: (− 2, −1, 1, 2, 4, 8, 16, 32, 64, 128) × 0.164 mJy beam^{-1}. The ∼360 pc east–west lobes at PA = 106° are seen in this image. Beam size: 0.43 arcsec × 0.30 arcsec at PA = −85.4°. (*Bottom*) 8.3 GHz *VLBA* image showing a ∼3 pc jet at PA = 130°. Contour levels: (− 2, −1, 1, 2, 4, 8, 16, 32, 64) × 0.239 mJy beam^{-1}. Beam size: 7.7 mas × 6.2 mas at PA = −4.9°.

Table 1. Details of the different data sets used for analysis in this paper.

Telescope	Project code	Observing date	Frequency	Array	Beam size
GMRT[a]	39_090	2020-11-15	735 MHz	–	5.48 arcsec × 3.0 arcsec, PA 54.6°
GMRTa	22_002	2012-06-09	325 MHz	–	12.1 arcsec × 9.8 arcsec, PA 37.6°
VLA[a]	17B-074	2017-11-04	5.5 GHz	B	1.02 arcsec × 0.89 arcsec, PA −5.8°
VLA	GL022	1998-02-17	5.0 GHz	A	0.43 arcsec × 0.30 arcsec, PA −85.4°
VLA[a]	AW126	1985-02-04	1.5 GHz	A	1.45 arcsec × 1.12 arcsec, PA 51.9°
VLBA	BC196J	2011-03-12	8.3 GHz	–	7.7 arcsec × 6.2 mas, PA −4.9°

Note.[a]Indicates the data sets that have been used for the BRATS spectral ageing analysis.

Table 2. Source parameters in the different data sets used in this paper.

Telescope	Frequency	Peak source intensity (mJy beam^{-1})	rms noise (μJy beam^{-1})	Total source intensity (mJy)	Source PA
GMRT	735 MHz	198	90	223 ± 22	34°
GMRT	325 MHz	249	128	286 ± 29	40°
VLA	5.5 GHz	42	9	57 ± 6	6°
VLA	5.0 GHz	54	54	79 ± 8	106°
VLA	1.5 GHz	61	82	93 ± 9	180°
VLBA	8.3 GHz	29	75	33 ± 3	130°

analysis in Section 3. The results and discussion follow in Sections 4 and 5, respectively, while the conclusions follow in Section 6. In this paper, we have adopted the following cosmological parameters: $H_0 = 73$ km s^{-1} Mpc^{-1}, $\Omega_{mat} = 0.27$, $\Omega_{vac} = 0.73$. Throughout the paper, spectral index α is defined such that flux density $S_\nu \propto \nu^\alpha$.

2 RADIO OBSERVATIONS AND DATA ANALYSIS

NGC 2639 was observed with the GMRT (Project code: 39_090) at 735 MHz (band 4) on 2020 November 15. The observing band consisted of a single spectral window, ranging from 550 to 950 MHz, across 4096 channels. The total on-source time was ≈36 min. 3C 147 was used as the amplitude calibrator and 0834+555 as the phase calibrator. Initial data editing and calibration were carried out using the CAPTURE continuum imaging pipeline for GMRT (Kale & Ishwara-Chandra 2021) on CASA (version 6.4; McMullin et al. 2007). The multiterm–multifrequency synthesis (MT-MFS; see Rau & Cornwell 2011, for more details) algorithm with two Taylor terms was used while imaging in CASA to account for wide-band related errors while deconvolving. Four rounds of phase-only self-calibration followed by four rounds of A&P (amplitude and phase) self-calibration were performed before the final image of NGC 2639 was created using the TCLEAN task in CASA. TCLEAN is the radio interferometric image reconstruction task that contains standard 'clean' based algorithms (e.g. Högbom 1974; Clark 1980) along with algorithms for multiscale and wideband image reconstruction. The final rms noise in the resulting image was ∼90 μJy beam^{-1}.

Calibrated data of NGC 2639 used by Sebastian et al. (2019) from the VLA B-array at 5.5 GHz, were also available. The data were imaged using the TCLEAN task in CASA using similar steps as above. Images obtained from archival VLA data at 1.5 GHz from 1985 and GMRT data at 325 MHz were used along with the above data sets for a spectral-ageing analysis. In addition to this, VLA images at 5 GHz from 1998 and VLBA images at 8.3 GHz from 2011, which were analyzed by Sebastian et al. (2019), were included in our analysis as well. These figures are included as insets in Fig. 2. Tables 1 and 2 include a summary of the data sets used along with their corresponding source properties. The flux densities were estimated using the CASA Viewer. We made rectangular boxes around the

extended emission using the drawing tool and noted the flux density values from the statistics tab of the region manager for the selected regions. The flux density errors were obtained through the formula $\sqrt{(\sigma_{rms} \times \sqrt{N_b})^2 + (\sigma_p \times S)^2}$, where σ_{rms} is the rms noise in the image, N_b is the number of beams that span the source area, σ_p is the percentage error on the absolute flux density scale (assumed to be a conservative 0.1 for the GMRT, VLA[1], and VLBA), and S is the source flux density (Kale, Shende & Parekh 2019).

3 SPECTRAL AGEING ANALYSIS USING BRATS

We used the Broad-band Radio Analysis ToolS (BRATS) software (Harwood et al. 2013; Harwood, Hardcastle & Croston 2015) to carry out a spectral ageing analysis of the different jet episodes in NGC 2639. We estimated the 'minimum energy' magnetic field (B_{min}) in the radio lobes assuming the equipartition of magnetic field and particle energy densities (e.g. Pacholczyk 1970) and used this as the magnetic field input in BRATS. We used the relations provided in O'Dea & Owen (1987) to calculate B_{min}. The volume-filling factor, ϕ, and the ratio of energy density of ions to electrons, η, was assumed to be unity. The upper and lower radio-band frequency cutoffs, ν_u and ν_l were taken to be 10 and 100 GHz, respectively. The lobes were assumed to be cuboidal, with the volume estimated using the relation $l \times w \times w$, where l and w are the lengths and widths of the full double-sided lobes, respectively. The input parameters, B_{min}, and other estimates are noted in Table 3.

3.1 GMRT north-east–south-west lobes

To perform a spectral age analysis using BRATS, a minimum of three images of the same size, resolution, and beam size at different frequencies are needed. From the calibrated GMRT band-4 data of NGC 2639, two sub-band images at central frequencies 643 and 810 MHz were obtained using TCLEAN with similar parameters as Section 2. These two images were smoothed and regridded using

---

[1]https://science.nrao.edu/facilities/vla/docs/manuals/oss/performance/fdscale

Table 3. Equipartition estimates. Lobes were assumed to be cuboidal (see Section 3) with a volume filling factor, $\phi = 1$, and the ratio of the energy density of ions to electrons, $\eta = 1$. The spectral index of each lobe was estimated by taking a spatial average over the lobe from the spectral index maps obtained through BRATS. The standard deviation in this is reported as the error. The sets of images used are the same as in Sections 3.1 and 3.2. The constant c_{12} which is a function of spectral index and radio-band frequency cutoffs has been obtained from Pacholczyk (1970).

Lobe	Frequency	Length (kpc)	Width (kpc)	Total flux density (mJy)	Spectral index α	c_{12}	L_{rad} (erg s^{-1})	B_{min} (G)
GMRT (both lobes)	735 MHz	9.0	3.1	223 ± 22	-0.2 ± 0.2	8.3×10^6	2.8×10^{40}	7.6×10^{-6}
VLA-south	5.5 GHz	0.83	0.5	1.42 ± 0.14	-0.53 ± 0.16	1.6×10^7	1.8×10^{38}	1.21×10^{-5}

Note. The source flux density/ source intensity errors were estimated using the same formula as in Section 2, with the appropriate regions selected.
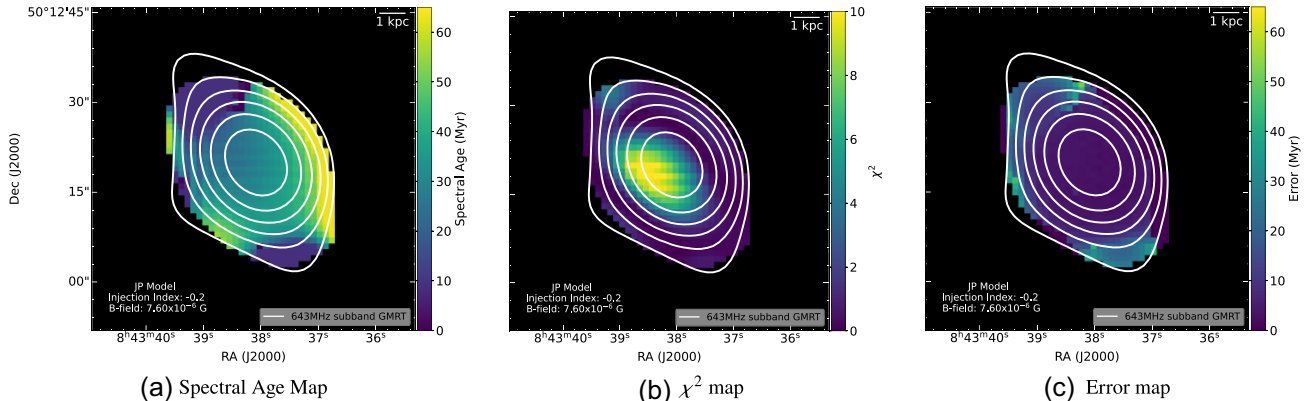

(a) Spectral Age Map (b) χ^2 map (c) Error map

Figure 3. *(Left)* Spectral age map of the GMRT $\sim$9 kpc lobes obtained using the smoothed and regridded images at 325, 643, and 810 MHz. *(Centre)* The χ^2 map of the fit to the JP model. *Right*: The map of the error in estimated spectral age. The mean spectral age of the jet is 34^{+4}_{-6} Myr (Note: The purple patches at the top and bottom of the spectral age map along, the central AGN region, and the yellow sliver on the right of the map were excluded from calculating mean due to poor fitting and high errors as can be seen in the central and right-hand panels.) Contour levels are of the 643 MHz GMRT sub-band image (see Section 3.1) at: (1, 2, 4, 8, 16, 32, 64) $\times$ 3.2 mJy beam^{-1}.

IMSMOOTH and IMREGRID in CASA to match the resolution, image size, and beam size of the lower resolution 325 MHz archival GMRT image. The final common restoring beam used was 12.1 arcsec $\times$ 9.8 arcsec at PA $= 37.6°$. In doing so, it was assumed that the lower resolution 325 MHz GMRT image contained the unresolved lobes which were seen at 735 MHz. The Jaffe-Perola (JP) model was used for fitting the synchrotron spectrum of the three radio images on BRATS (see Harwood et al. 2013, 2015, for details). A 5σ detection threshold was used with only the source regions selected. The injection index was chosen as -0.2 as this was the approximate spectral index of the core. In doing so, it was assumed that electrons are being accelerated near the centre as opposed to the progressing edges of the lobes as in Fanaroff-Riley Class II (FRII) radio galaxies (e.g. Mahatma et al. 2020). This was because no hotspots were observed in any of the radio images and the source resembles an FRI-type or Seyfert-like jet. The magnetic field (BFIELD) was set to the equipartition value of 7.6×10^{-6} G and the spectral age map was obtained using the FITJPMODEL task on BRATS with levels = 5 and Myrs = 60.

3.2 VLA north–south lobes

From the calibrated 5.5 GHz full-band VLA data of NGC 2639, two sub-band images at central frequencies 5 and 6 GHz were obtained using TCLEAN. These two images were smoothed and regridded using IMSMOOTH and IMREGRID on CASA to match the resolution, image size, and beam size of the lower resolution 1.5 GHz archival VLA image, in which only the southern lobe was visible. The final common restoring beam used was 1.45 arcsec $\times$ 1.12 arcsec at PA $=51.9°$. With the core and southern lobe regions selected and

a 5σ detection threshold, the synchrotron spectrum of the radio images were fitted with the JP model on BRATS. The injection index was again chosen to be -0.2 and the magnetic field was taken as 1.2×10^{-5} G from the equipartition estimate. The spectral age map was obtained from the FITJPMODEL task with levels = 5 and Myr = 20.

4 RESULTS

Fig. 1 shows the total radio intensity image contours at 325 MHz, 735 MHz, and 5.5 GHz superimposed on the SDSS r band colour map of NGC 2639. Fig. 2 shows the total intensity image from GMRT, as well as the total intensity images from VLA and VLBA. The new north-east–south-west radio lobes, which were previously not detected in GHz frequency observations with the VLA, are clearly seen in Figs 1 and 2. The linear extents of each of these lobes are $\sim$4.5 kpc. The PA of the host galaxy disc is 136° whereas the PA of the north-east–south-west lobes is 34°. The surface discontinuity of the outermost contour of this lobe is $\sim$7 times the rms noise. The PA of the VLA north–south lobes is 6° and that of the east–west lobes is 106°. The surface discontinuities of the outermost contours for the two sets of lobes are $\gtrsim$3 times the rms noise. The GMRT image at 325 MHz do not resolve these lobes clearly but detects additional radio emission from the host galaxy itself (see Fig. 1).

4.1 Episodic activity and AGN jet duty cycle

Using multifrequency arcsec-scale radio data, we have carried out a spectral ageing analysis using BRATS, as described in Section 3. Figs 3 and 4 show the spectral age maps of the GMRT and VLA
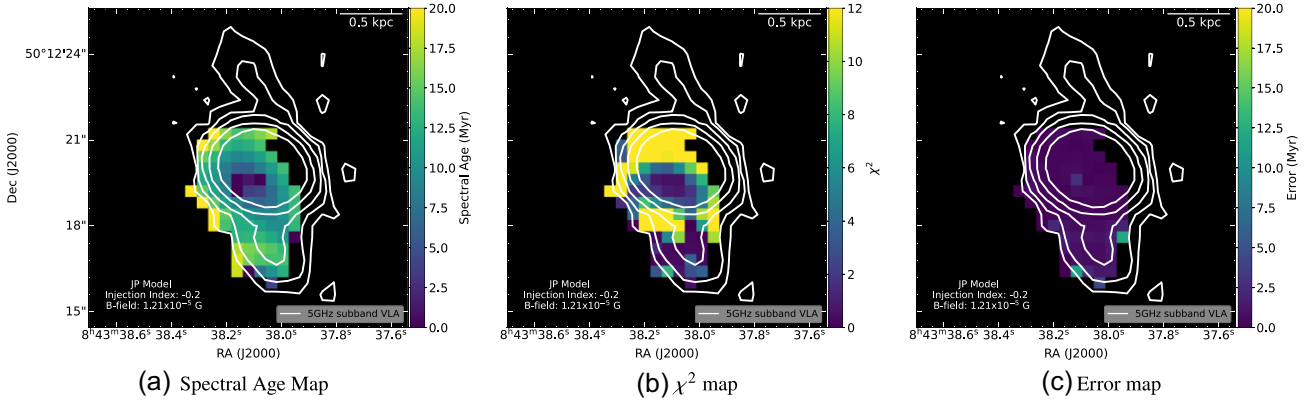
Figure 4. (*Left*) Spectral age map of the VLA core and the ~0.8 kpc south lobe obtained using the smoothed and regridded images at 1.4, 5.0, and 6.0 GHz. (*Centre*) The χ^2 map of the fit to the JP model. (*Right*) The map of the error in estimated spectral age. The mean spectral age of the southern lobe is $12^{+1.7}_{-1.4}$ Myr and the mean spectral age of the core is $2.8^{+0.7}_{-0.5}$ Myr (Note: The yellow regions with high χ^2 in the χ^2 map were excluded from calculating mean.) Contour levels are of the 5 GHz VLA sub-band image (see Section 3.2) at: (1, 3, 9, 27, 81) × 0.036 mJy beam^{-1}.
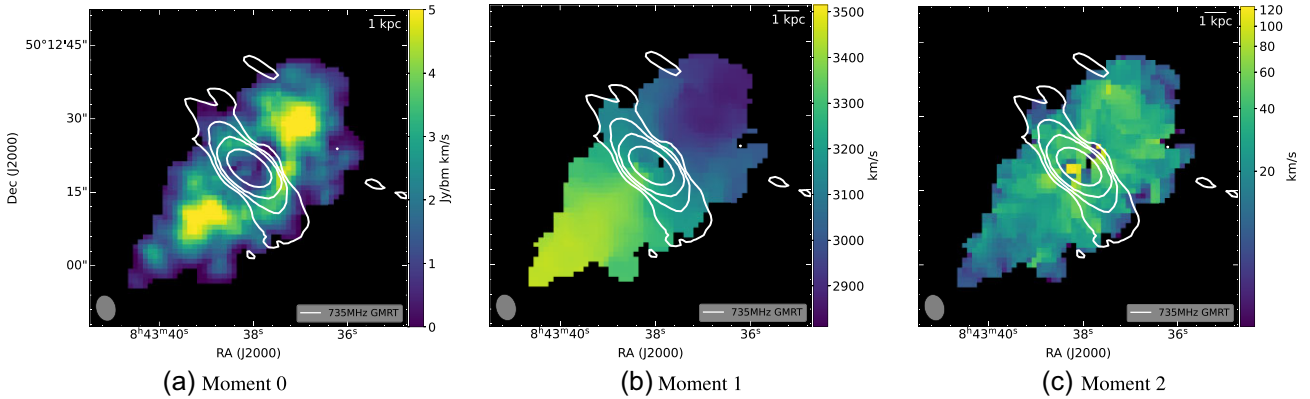

Figure 5. (*Left*) Moment 0 image of the CO(1–0) molecular gas emission line from the CARMA EDGE survey, overlaid with the 735 MHz GMRT radio contours. This image represents the integrated CO intensity and shows a deficiency of CO(1–0) molecular gas in the central ~6 kpc. (*Centre*) The Moment 1 image representing the velocity of the CO molecular gas. The distribution shows uniform rotation. (*Right*) The Moment 2 image with the same contour levels, represents the velocity dispersion of the CO molecular gas. Higher velocity dispersion values are observed around the jet edges. Common contour levels are (1, 2, 4, 32) × 0.6 mJy beam^{-1}.

lobes, respectively. The mean spectral age of the north-east–south-west GMRT lobes is 34^{+4}_{-6} Myr, that of the southern VLA lobe is $11.8^{+1.7}_{-1.4}$ Myr, and that of the core is $2.8^{+0.7}_{-0.5}$ Myr. The ages of the southern lobe and core obtained are comparable to the electron lifetime estimates obtained by Sebastian et al. (2019) of 12−16 and 0.8 Myr, respectively. The PA offset of ~30° between the north-east–south-west GMRT lobes and the north-south VLA lobes put together with the spectral ages, which are deduced from the steepness of the radio spectrum, indicate that the two are distinct jet episodes. Thus, the GMRT, VLA, and VLBA data show that NGC 2639 is a candidate for an AGN with four jet episodes. We note that it is possible that the VLBA jet is feeding the east–west VLA lobes (e.g. Kharb et al. 2010), which could reduce the number of episodes to three. However, in view of the ~30° PA offset between the VLBA jet and the VLA east–west lobes, we will continue to refer to four jet episodes in NGC 2639. The spectral age results indicate that the jets were launched 9–22 Myr apart with the 9 kpc, north-east–south-west, GMRT jets being launched first followed by the 1.5 kpc, north–south VLA jets, and the 360 pc east–west VLA jets, respectively, where the age of the core in Fig. 4 is taken

to be indicative of the age of the 360 pc long east–west VLA jet. Defining the AGN jet duty cycle as $\epsilon = t_{on}/(t_{on} + t_{off})$ (see Clarke & Burns 1991), we use the ages of the VLA east–west lobes and north–south lobes to obtain $\epsilon = 11.8/(11.8 + 9.0) = 0.57$. Similarly, using the ages of the VLA north–south lobes and the GMRT lobes, we obtain $\epsilon = 34.0/(34.0 + 22.2) = 0.60$. The AGN jet duty cycle in NGC 2639 is, therefore, ~60 per cent. These data, however, cannot directly answer whether other AGN activity episodes that might not have produced radio jets occurred in this source. For instance, these data cannot rule out episodic 'wind' activity that may be unrelated to the radio jets (e.g. King & Pounds 2015), leaving an overall uncertainty in the true AGN duty cycle in NGC 2639.

4.2 Looking for the jet-gas connection

The left-hand panel of Fig. 5 shows the Moment-0 image of the CO(1–0) molecular gas emission line in NGC 2639 from the CARMA-EDGE survey (Bolatto et al. 2017). This image represents the integrated CO intensity and clearly shows the deficit of CO(1–0)
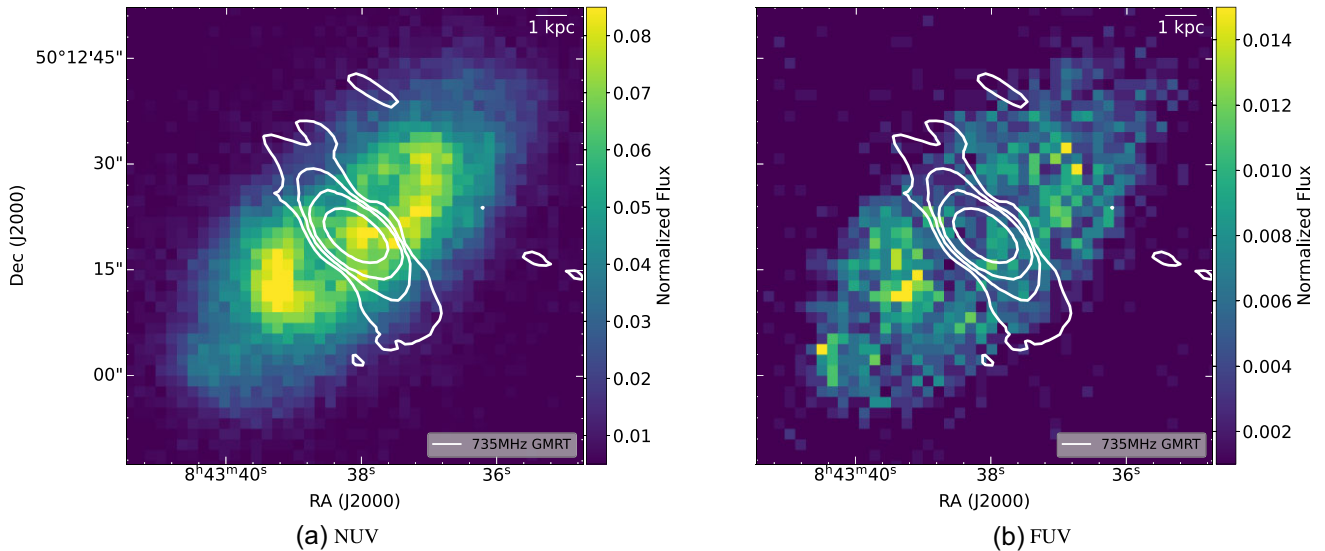
Figure 6. *(Left)* NUV and *(Right)* FUV image of NGC 2639 from *GALEX* overlaid with the 735 MHz GMRT radio contours at $(1, 2, 4, 32) \times 0.6$ mJy beam^{-1}. The central ∼6 kpc shows a relative deficiency of NUV emission, barring emission from the AGN, indicating a lack of star formation. The AGN is likely obscured in the FUV image due to dust.

molecular gas emission in the central ∼6 kpc region; the integrated intensity is 5–7 times higher in the ring than in the central regions. Using the same CO(1–0) map, Ellison et al. (2021) obtained the molecular gas surface densities (Σ_{H_2}) for NGC 2639 using the CO-to-H$_2$ conversion factor $\alpha_{CO} = 4.3$ M$_\odot$ pc^{-2} (K km s^{-1})$^{-1}$. Selecting for AGN and star-forming spaxels using optical line widths from the Calar Alto Legacy Integral Field Area (CALIFA; Sánchez et al. 2012) survey, they concluded that the molecular gas fractions of central AGN regions are ∼2 lower than in star-forming regions, suggesting that the AGN has affected the central molecular gas reservoir. It is worth noting that in comparison to the other three galaxies in their sample, NGC 2639 exhibited the highest AGN luminosity and a more pronounced lack of molecular gas. While it is possible that the hard ionizing radiation field from the AGN or nuclear star formation can affect the CO spectral line energy distributions, and thereby the low CO transitions, it cannot explain the observed velocity dispersion values (see ahead). Thus, as in Ellison et al. (2021), we continue to treat the lack of CO(1–0) molecular gas emission as a lack of molecular gas. Here, and in other sections, by molecular gas we primarily mean H$_2$ gas traced by the CO(1–0) emission line.

The CO(1–0) Moment 1 map of NGC 2639 (central panel of Fig. 5) suggests a rotating molecular gas that appears to be largely regular; clear signatures of turbulence are not directly observed. The Moment 2 map, however, reveals slightly higher velocity-dispersion values (of the order of 100 km s^{-1}) around the GMRT jet edges (see right-hand panel of Fig. 5). This could suggest that the jet does impact the molecular gas by injecting turbulent kinetic energy into the medium. If the molecular gas ring is a result of gas being pushed aside due to the radio jet in NGC 2639, we can estimate the *PV* (pressure times volume) amount of work required to create such a cavity. Using the typical temperature (*T*) and density (*n*) of the molecular medium of the galactic interstellar medium (ISM), i.e. $T \simeq 20$ K, and $n > 10^3$ cm^{-3} (see Brinks 1990), and assuming it to be similar in NGC 2639, we can estimate the molecular gas pressure as $P = nk_B T$, where k_B is the Boltzmann constant. For the molecular gas ring radius of 3 kpc, the volume of the disc-like cavity is 1.25×10^{66} cm^3 and the *PV* work required is $> 3.44 \times 10^{54}$ erg. It is worth noting that the temperature in the ISM may be higher in the vicinity of the AGN,

which will increase the required amount of work. However, a much higher temperature will lead to photodissociation of the molecules themselves (Omont 2007).

We can also estimate the jet mechanical powers using the relations derived for low luminosity AGN by Merloni & Heinz (2007). Using only the lobe flux densities[2] at 5 GHz (∼13 mJy), we find that the jet power for the east–west VLA lobes is 7.7×10^{42} erg s^{-1} and the time-averaged power (for a spectral age of 2.8 Myr) is 6.8×10^{56} erg. Similarly, for the north–south VLA lobes having a flux density of ∼1.4 mJy, the 5.5 GHz jet power is 1.3×10^{42} erg s^{-1}, and its time-averaged power (over 12 Myr) is 4.9×10^{56} erg. Finally, using an average lobe spectral index of -0.3 and a lobe flux density of ∼16 mJy, the jet power for the north-east–south-west GMRT lobes is 5.7×10^{42} erg s^{-1}, and its time-averaged power (over 34 Myr) is 6.1×10^{57} erg. Therefore, only ∼0.5 per cent of the east–west jet power is sufficient to push aside the molecular gas in NGC 2639; these numbers are ∼0.7 per cent for the north–south jets and ∼0.06 per cent for the north-east–south-west jets, respectively.

The accumulation of clouds of dense molecular gas around the nucleus of this water maser galaxy seems necessary for the water megamaser to be produced (Martin et al. 1989; Krause et al. 1990). However, Raluy, Planesas & Colina (1998) found no apparent relation between the maser luminosity and the surface density or the total content of molecular gas in the innermost kpc-scale galactic regions. The sole correlation found involves the surface density of molecular gas in the inner areas of galaxies, indicating an anticorrelation with the rate of change in maser intensity. This finding suggests that the nuclear jets interacting with matter clouds surrounding the active nucleus at different scales may generate or boost maser emission. Braatz et al. (2003); Pesce (2018) have noted that NGC 2639 shows evidence for accelerating systemic features, but no high-velocity features have ever been observed for this system.

---

[2]Lobe flux density is the total flux density minus the core flux density.

Table 4. Estimates of star formation rate in NGC 2639 using different tracers.

SFR ($M_\odot$ yr^{-1})	Telescope	SFR indicator	Aperture (arcsec)	Σ_{SFR} ($M_\odot$ yr^{-1} kpc^{-2})	Reference
0.92	*Nickel 1.0 m* telescope at *Lick Observatory*	Hα	73.5	0.00099	(1)
1	*Spitzer Space Telescope*	IR	40	0.0036	(2)
0.57	*Calar Alto* 3.5 m telescope	Hα	36	0.0026	(3)

Notes. References: (1) Theios, Malkan & Ross (2016) using the relation, SFR ($M_\odot$ yr^{-1}) $= 5.37 \times 10^{-42}$ L$_{H\alpha}$ (erg s^{-1}), where L$_{H\alpha}$ $= 10^{41.23}$ (erg s^{-1}) for NGC 2639
(2) Sebastian et al. (2019) using the CLUMPYDREAM code.
(3) Catalán-Torrecilla et al. (2015) using the Hα line luminosity from the CALIFA survey.

4.3 Indications of star formation quenching

The *Galaxy Evolution Explorer* (*GALEX*) data on NGC 2639 shows a relative deficiency of near-UV (NUV, $\lambda_{eff} = 2267$ Å) emission from the central $\sim$6 kpc of the galaxy (see Fig. 6, left-hand panel), barring the emission from the AGN itself. The far-UV (FUV, $\lambda_{eff} = 1516$ Å) image (Fig. 6, right-hand panel) also shows a similar deficiency of emission but is not as clear as in the NUV, which could be due to the presence of dust. The absence of the AGN in the FUV image, however, would be consistent with its type 2 classification and its obscuration from a dusty torus (see e.g Dewangan et al. 2021). We note that the NUV band is one of the most direct tracers of stars formed over the last $10-200$ Myr (Kennicutt & Evans 2012). The central void in the *GALEX* images, therefore, is consistent with the suggestion of star formation quenching in the central few kpc in NGC 2639. We attempt to quantify this further ahead.

The global Schmidt law for star-forming galaxies has been given by Kennicutt (1998) as

$$\Sigma_{SFR} = (2.5 \pm 0.7) \times 10^{-4} \left(\frac{\Sigma_{gas}}{1\ M_\odot\ pc^{-2}} \right)^{1.4 \pm 0.15} M_\odot\ yr^{-1}\ kpc^{-2},$$

where the SFR surface density, Σ_{SFR}, can be derived from gas surface density, Σ_{gas}. For NGC 2639, using $\Sigma_{gas} \equiv \Sigma_{H_2} = 21\ M_\odot\ pc^{-2}$ for a region of 4.8 kpc, which is the linear size of the antenna beam of the *Institut de radioastronomie millimétrique* (IRAM) 30 m telescope at the distance of the galaxy (Raluy et al. 1998), Σ_{SFR} should be 0.0177 $M_\odot$ yr^{-1} kpc^{-2}. The SFR surface density can also be computed from the SFR estimates using the following expression:

$$\Sigma_{SFR} = \frac{SFR}{\pi a^2 \left(\frac{d}{206265} \right)^2}, \quad (2)$$

where the parameter *a* corresponds to the semi-major axis of the telescope aperture in arcsec and *d* is the distance to the galaxy in Mpc (Catalán-Torrecilla et al. 2015). Several estimates for SFR have been derived for NGC 2639 in the literature. Table 4 provides the estimates of Σ_{SFR} obtained using different SFR tracers. The telescope details for individual tracers are also provided. These estimates of Σ_{SFR} lie below the global Schmidt best-fitting line for star-forming galaxies by a factor of $5-18$, consistent with star formation quenching in NGC 2639. Kennicutt (1998) have noted that the scatter in this relation is ± 0.3 dex with individual sources deviating by as much a factor as 7. These results are consistent with the *GALEX* NUV image of NGC 2639, showing a deficit in recent star formation in the central $\sim$6 kpc region.

5 DISCUSSION

NGC 2639 is a member of the non-interacting spiral (NIS) galaxy sample considered for a stellar population modeling study by Zaragoza-Cardiel et al. (2018) and has been identified as such by Gil de Paz et al. (2007). The stars of NGC 2639 are relatively undisturbed and are in uniform motion, as seen in the line-of-sight velocity map obtained from the Calar Alto Legacy Integral Field Area (CALIFA) survey (de Amorim et al. 2017). According to Sebastian et al. (2019), the multiple radio lobes seen in NGC 2639 are due to minor mergers that did not disrupt the morphology of the host galaxy. The misaligned jets could be the result of new accretion discs formed from mergers, with jet directions conserving the angular momentum of the inflowing gas (e.g. Kharb et al. 2006; Volonteri, Sikora & Lasota 2007). This scenario is consistent with NGC 2639 having a large bulge component surrounding the nucleus (Cox et al. 2007) as gravitational forces and torques that result from mergers disrupt the orbital path of stars causing randomized bulge orbits. Thus, if the minor merger scenario were true, the spectral age results of the multiple lobes indicate that minor mergers occurred every $9-22$ Myr apart in the last $\sim$30 Myr.

The expected minor merger rate for a galaxy like NGC 2639 (redshift of 0.01113 and stellar mass of $1.48 \times 10^{11}\ M_\odot$) is $\sim$13 Myr following the work of Conselice et al. (2022), who used observational data from the Redshift Evolution and Formation in Extragalactic systems (REFINE) survey. We used their minor mergers best-fitting line (with stellar mass ratios of 1:10) to obtain this estimate. The estimate of $\sim$10 Myr also matches the estimates obtained via theoretical studies as well as galaxy-merger simulations (Hopkins et al. 2010; Capelo et al. 2015). It would therefore be fair to conclude that at least three minor mergers have taken place in the lifetime of NGC 2639. Each of these mergers may have resulted in the formation of a new accretion disc with no memory of the previous accretion disc direction, primarily driven by the angular momentum of the infalling material itself (e.g. Kharb et al. 2006). Accretion through these discs would have resulted in the several differently-oriented jet episodes that are observed in NGC 2639. As noted in Section 4.2, each of these jet episodes have sufficient mechanical power to displace the CO and H$_2$ molecular gas from the central few kpc of the host galaxy.

The early-type galaxy and LINER, NGC 1266, shows the presence of a CO molecular outflow, no signatures of galaxy interactions, and a possible radio jet at 1.4 GHz (Alatalo et al. 2011). There is also a centrally concentrated molecular component which is different from the case of NGC 2639, where instead, a central deficiency is observed. Alatalo et al. (2011) suggest that the jet in NGC 1266 is sufficient to drive the molecular outflow using only 2 per cent of its total power at 1.4 GHz. We note, however, that multiresolution, multifrequency radio observations are required to truly rule out the existence of multiple jet episodes in NGC 1266. Nesvadba et al. (2021) detected a CO(1–2) molecular gas ring through *ALMA* observations in the nearby spiral galaxy J2345−0449 with large kpc-scale radio jets. Interestingly, the inner radius of the CO gas ring corresponds to 4.2×2.2 kpc, very similar to what is observed in NGC 2639. Moreover, they find that the molecular gas outflow in J2345−0449

has a kinetic energy of 1.3×10^{57} erg. Again, only a small fraction of the jet kinetic power in J2345−0449 (and as it happens in NGC 2639) can suffice to drive molecular gas outflows. It is worth noting that the radio source in J2345−0449 is also a restarted double–double radio galaxy.

The simulations performed by Mukherjee et al. (2016, 2017) show that low-power jets ($P_{jet} \lesssim 10^{44}$ erg s^{-1}) have a more pronounced impact on ISM evolution in comparison to high-power jets ($P_{jet} \gtrsim 10^{45}$ erg s^{-1}) due to their longer trapping time and therefore the constant stirring of the turbulent ISM, ultimately leading to a suppression of star formation. The low-power jets also evacuate $\gtrsim 1$ kpc cavities, with cavity sizes increasing with decreasing power. The simulations show that only a small percentage of the dense gas mass is ejected by jets. However, the injection of turbulent kinetic energy by the jet into the ISM may temporarily suppress star formation in the remaining gas, as observed by Alatalo et al. (2015). This suppression is temporary as the ejected mass eventually falls back into the ISM and may become available for star formation after a few tens of Myr.

Recent simulations of Mukherjee et al. (2018) and Meenakshi et al. (2022) have demonstrated that jet–ISM coupling is sensitive to the relative orientation of the jet w.r.t. the gas disc, as well as the age of the jet. It is stronger for the jets, which are oriented at $\leq 45°$ w.r.t the gas disc and young (≤ 2 Myr). Thus, the absence of CO(1–0) emission in the inner 6 kpc region of NGC 2639, the relatively small values of Σ_{SFR} observed compared to the Schmidt law for star-forming galaxies, and the high CO(1–0) velocity dispersion seen in the central regions, together paint a complex picture of 'negative AGN feedback' in NG 2639. Given the directional nature of the jets in NGC 2639, we speculate that the jets restarting repeatedly on time-scales comparable to the fall-back time of the gas is an important factor in launching multiple local outflows, and maintaining a turbulent ISM, regulating star formation. NGC 2639 is thus, another potential candidate to add to the increasing number of observed instances (e.g. Alatalo et al. 2015; Venturi et al. 2021; Girdhar et al. 2022) where low-power radio jets have been identified as a significant source of feedback.

6 CONCLUSIONS

The Seyfert galaxy NGC 2639 exhibits four episodes of AGN jet activity as evidenced by 735 MHz, 5.5 GHz, and 8.3 GHz frequency observations via the GMRT, VLA, and the VLBA telescopes, respectively. Using the spectral ageing software BRATS, we derive the ages of the three pairs of lobes to be respectively, 34^{+4}_{-6}, $11.8^{+1.7}_{-1.4}$, and $2.8^{+0.7}_{-0.5}$ Myr, with the GMRT lobes being the oldest (we did not derive an age for the VLBA jet). Using the 'on' and 'off' times of these jets/lobes, the AGN jet duty cycle in NGC 2639 is ∼60 per cent. NGC 2639 also shows a deficiency of molecular gas in its central ∼6 kpc region. Less than 1 per cent of the jet mechanical power for each of the jet episodes taken individually, is sufficient to move the molecular gas. However, given the directionality of each jet episode, the creation and maintenance of a doughnut-shaped hole in the molecular gas in the galactic centre likely required multiple jets restarting on time-scales comparable to the fall-back times of ejected molecular gas. Like the CO(1–0) emission line image, the *GALEX* NUV image also shows a relative deficiency of star formation in the last 200 Myr in the inner ∼6 kpc region. Additionally, the SFR surface density is lower by a factor of $5-18$ compared to the global Schmidt law of star-forming galaxies. The results suggest that the central regions of NGC 2639 are influenced by multiple

low-power jets, which could be playing a key role in regulating star formation. This would make NGC 2639 a case of a RQAGN showing episodic jet activity and possible signatures of jet-driven AGN feedback.

REFERENCES

Alatalo K. et al., 2011, ApJ, 735, 88
Alatalo K. et al., 2015, ApJ, 798, 31
Alexander D. M., Hickox R. C., 2012, New Astron. Rev., 56, 93
Antonucci R., 1993, ARA&A, 31, 473
Baldi R. D. et al., 2018, MNRAS, 476, 3478
Baum S. A., O'Dea C. P., Dallacassa D., de Bruyn A. G., Pedlar A., 1993, ApJ, 419, 553
Behar E., Baldi R. D., Laor A., Horesh A., Stevens J., Tzioumis T., 2015, MNRAS, 451, 517
Berrier J. C. et al., 2013, ApJ, 769, 132
Bolatto A. D. et al., 2017, ApJ, 846, 159
Bower R. G., Benson A. J., Crain R. A., 2012, MNRAS, 422, 2816
Braatz J. A., Wilson A. S., Henkel C., 1994, ApJ, 437, L99
Braatz J. A., Wilson A. S., Henkel C., Gough R., Sinclair M., 2003, ApJS, 146, 249
Brinks E., 1990, in Thronson Harley A. J., Shull J. M.eds, Astrophysics and Space Science Library Vol. 161, The Interstellar Medium in Galaxies. p. 39
Capelo P. R., Volonteri M., Dotti M., Bellovary J. M., Mayer L., Governato F., 2015, MNRAS, 447, 2123
Catalán-Torrecilla C. et al., 2015, A&A, 584, A87
Cattaneo A., Best P. N., 2009, MNRAS, 395, 518
Clark B. G., 1980, A&A, 89, 377
Clarke D. A., Burns J. O., 1991, ApJ, 369, 308
Conselice C. J., Mundy C. J., Ferreira L., Duncan K., 2022, ApJ, 940, 168
Costa T., Rosdahl J., Sijacki D., Haehnelt M. G., 2018, MNRAS, 479, 2079
Cox T. J., Younger J., Hernquist L., Hopkins P. F., 2007, Proc. Int. Astron. Union, 3, 63
Croton D. J., 2009, MNRAS, 394, 1109
de Amorim A. L. et al., 2017, MNRAS, 471, 3727
Dewangan G. C., Tripathi P., Papadakis I. E., Singh K. P., 2021, MNRAS, 504, 4015
Elitzur M., Ho L. C., Trump J. R., 2014, MNRAS, 438, 3340
Ellison S. L. et al., 2021, MNRAS, 505, L46
Fabian A. C., 2012, ARA&A, 50, 455
Faucher-Giguère C.-A., Quataert E., 2012, MNRAS, 425, 605
Ferrarese L., Merritt D., 2000, ApJ, 539, L9
Gallimore J. F., Axon D. J., O'Dea C. P., Baum S. A., Pedlar A., 2006, AJ, 132, 546
Gil de Paz A. et al., 2007, ApJS, 173, 185
Girdhar A. et al., 2022, MNRAS, 512, 1608

Hardcastle M. J., Croston J. H., 2020, New Astron. Rev., 88, 101539
Harrison C. M., 2017, Nat. Astron., 1, 0165
Harwood J. J., Hardcastle M. J., Croston J. H., Goodger J. L., 2013, MNRAS, 435, 3353
Harwood J. J., Hardcastle M. J., Croston J. H., 2015, MNRAS, 454, 3403
Heckman T. M., Best P. N., 2014, ARA&A, 52, 589
Hickox R. C., Alexander D. M., 2018, ARA&A, 56, 625
Ho L. C., 2008, ARA&A, 46, 475
Ho L. C., 2009, ApJ, 699, 626
Högbom J. A., 1974, A&AS, 15, 417
Hopkins P. F. et al., 2010, ApJ, 724, 915
Hota A., Saikia D. J., 2006, MNRAS, 371, 945
Irwin J. A. et al., 2016, MNRAS, 464, 1333
Jurlin N. et al., 2020, A&A, 638, A34
Kale R., Ishwara-Chandra C. H., 2021, Exp. Astron., 51, 95
Kale R., Shende K. M., Parekh V., 2019, MNRAS, 486, L80
Kellermann K. I., Condon J. J., Kimball A. E., Perley R. A., Ivezić Ž., 2016, ApJ, 831, 168
Kennicutt Robert C. J., 1998, ApJ, 498, 541
Kennicutt R. C., Evans N. J., 2012, ARA&A, 50, 531
Khachikian E. Y., Weedman D. W., 1974, ApJ, 192, 581
Kharb P., O'Dea C. P., Baum S. A., Colbert E. J. M., Xu C., 2006, ApJ, 652, 177
Kharb P., Hota A., Croston J. H., Hardcastle M. J., O'Dea C. P., Kraft R. P., Axon D. J., Robinson A., 2010, ApJ, 723, 580
Kharb P., Das M., Paragi Z., Subramanian S., Chitta L. P., 2015, ApJ, 799, 161
Kharb P., Subramanian S., Das M., Vaddi S., Paragi Z., 2021, ApJ, 919, 108
King A., Pounds K., 2015, ARA&A, 53, 115
Koulouridis E., 2014, A&A, 570, A72
Koulouridis E. et al., 2016, A&A, 586, A3
Krause M., Cox P., Garcia-Barreto J. A., Downes D., 1990, A&A, 233, L1
Lacerda E. A. D., Sánchez S. F., Cid Fernandes R., López-Cobá C., Espinosa-Ponce C., Galbany L., 2020, MNRAS, 492, 3073
Lalakos A. et al., 2022, ApJ, 936, L5
Mahatma V. H., Hardcastle M. J., Croston J. H., Harwood J., Ineson J., Moldon J., 2020, MNRAS, 491, 5015
Mahony E. K., Morganti R., Emonts B. H. C., Oosterloo T. A., Tadhunter C., 2013, MNRAS, 435, L58
Malzac J., Beloborodov A. M., Poutanen J., 2001, MNRAS, 326, 417
Markoff S., Nowak M. A., Wilms J., 2005, ApJ, 635, 1203
Martin P., Roy J.-R., Noreau L., Lo K. Y., 1989, ApJ, 345, 707
McMullin J. P., Waters B., Schiebel D., Young W., Golap K., 2007, in Shaw R. A., Hill F., Bell D. J.eds, Astron. Soc. Pac. Conference Series Vol. 376, Astronomical Data Analysis Software and Systems XVI, San Francisco
McNamara B. R., Nulsen P. E. J., 2012, New J. Phys., 14, 055023
Meenakshi M., Mukherjee D., Wagner A. Y., Nesvadba N. P. H., Morganti R., Janssen R. M. J., Bicknell G. V., 2022, MNRAS, 511, 1622
Merloni A., Heinz S., 2007, MNRAS, 381, 589
Merloni A., Heinz S., 2008, MNRAS, 388, 1011
Mezcua M., Prieto M. A., 2014, ApJ, 787, 62
Morganti R., 2017, Front. Astron. Space Sci., 4, 42

Mukherjee D., Bicknell G. V., Sutherland R., Wagner A., 2016, MNRAS, 461, 967
Mukherjee D., Bicknell G. V., Sutherland R., Wagner A., 2017, MNRAS, 471, 2790
Mukherjee D., Bicknell G. V., Wagner A. Y., Sutherland R. S., Silk J., 2018, MNRAS, 479, 5544
Nagar N. M., Falcke H., Wilson A. S., 2005, A&A, 435, 521
Nesvadba N. P. H. et al., 2021, A&A, 654, A8
Netzer H., 2015, ARA&A, 53, 365
O'Dea C. P., Owen F. N., 1987, ApJ, 316, 95
Omont A., 2007, Rep. Prog. Phys., 70, 1099
Orr M. J. L., Browne I. W. A., 1982, MNRAS, 200, 1067
Pacholczyk A. G., 1970, Radio Astrophysics. Nonthermal Processes in Galactic and Extragalactic Sources. Freeman, San Francisco
Padovani P. et al., 2017, A&AR, 25, 2
Panessa F., Baldi R. D., Laor A., Padovani P., Behar E., McHardy I., 2019, Nat. Astron., 3, 387
Pesce D. W., 2018, PhD thesis, University of Virginia
Raluy F., Planesas P., Colina L., 1998, A&A, 335, 113
Rau U., Cornwell T. J., 2011, A&A, 532, A71
Readhead A. C. S., Cohen M. H., Blandford R. D., 1978, Nature, 272, 131
Rees M. J., 1984, ARA&A, 22, 471
Saikia D. J., 2022, JA&A, 43, 97
Saikia D. J., Jamrozy M., 2009, Bull. Astron. Soc. India, 37, 63
Sánchez S. F. et al., 2012, A&A, 538, A8
Sanders R. H., 1984, A&A, 140, 52
Schmidt M., Green R. F., 1983, ApJ, 269, 352
Sebastian B., Kharb P., O'Dea C. P., Gallimore J. F., Baum S. A., 2019, MNRAS, 490, L26
Sebastian B., Kharb P., O'Dea C. P., Gallimore J. F., Baum S. A., 2020, MNRAS, 499, 334
Shabala S. S., Jurlin N., Morganti R., Brienza M., Hardcastle M. J., Godfrey L. E. H., Krause M. G. H., Turner R. J., 2020, MNRAS, 496, 1706
Shankar F., Cavaliere A., Cirasuolo M., Maraschi L., 2008, ApJ, 676, 131
Singh V., Ishwara-Chandra C. H., Wadadekar Y., Beelen A., Kharb P., 2015, MNRAS, 446, 599
Soifer B. T., Sanders D. B., Madore B. F., Neugebauer G., Danielson G. E., Elias J. H., Lonsdale C. J., Rice W. L., 1987, ApJ, 320, 238
Sweet S. M., Fisher D., Glazebrook K., Obreschkow D., Lagos C., Wang L., 2018, ApJ, 860, 37
Terashima Y., Iyomoto N., Ho L. C., Ptak A. F., 2002, ApJS, 139, 1
Thean A., Pedlar A., Kukula M. J., Baum S. A., O'Dea C. P., 2001, MNRAS, 325, 737
Theios R. L., Malkan M. A., Ross N. R., 2016, ApJ, 822, 45
Venturi G. et al., 2021, A&A, 648, A17
Volonteri M., Sikora M., Lasota J.-P., 2007, ApJ, 667, 704
Wilson A. S., Braatz J. A., Henkel C., 1995, ApJ, 455, L127
Wong O. I. et al., 2016, MNRAS, 460, 1588
Xanthopoulos E., Thean A. H. C., Pedlar A., Richards A. M. S., 2010, MNRAS, 404, 1966
Zaragoza-Cardiel J., Smith B. J., Rosado M., Beckman J. E., Bitsakis T., Camps-Fariña A., Font J., Cox I. S., 2018, ApJS, 234, 35

This paper has been typeset from a TEX/LATEX file prepared by the author.